

# Automatic intraluminal scanning with a steerable endoscopic optical coherence tomography catheter for gastroenterology applications

Oscar Caravaca-Mora<sup>a,b</sup>, Philippe Zanne<sup>a</sup>, Guiqiu Liao<sup>a,c</sup>,  
Natalia Zulina<sup>a</sup>, Lucile Heroin<sup>a,d</sup>, Lucile Zorn<sup>a</sup>, Michel De Mathelin<sup>a</sup>,  
Benoit Rosa<sup>a</sup>, Florent Nageotte<sup>a</sup>, and Michalina J. Gora<sup>a,e,\*</sup>

<sup>a</sup>UMR 7357 CNRS – University of Strasbourg, ICube Laboratory, Strasbourg, France

<sup>b</sup>Wellman Center for Photomedicine, Boston, Massachusetts, United States

<sup>c</sup>University of Verona, Altair Laboratory, Verona, Italy

<sup>d</sup>Hôpitaux universitaires de Strasbourg, Gastroenterology Department, Strasbourg, France

<sup>e</sup>Wyss Center for Bio and Neuroengineering, Geneva, Switzerland

## Abstract

**Significance:** Endoscopic optical coherence tomography (OCT) enables real-time optical biopsy of human organs. Endoscopic probes require miniaturization of optics, which in turn limits field of view. When larger imaging areas are needed such as in the gastrointestinal tract, the operator must manually scan the probe over the tissue to extend the field of view, often resulting in an imperfect scanning pattern and increased risk of missing lesions. Automatic scanning has the potential to extend the field of view of OCT, allowing the user to focus on image interpretation during real-time observations.

**Aim:** This work proposes an automatic scanning using a steerable OCT catheter integrated with a robotized interventional flexible endoscope. The aim is to extend the field of view of a low-profile OCT probe while improving scanning accuracy and maintaining a stable endoscope's position during minimally invasive treatment of colorectal lesions.

**Approach:** A geometrical model of the steerable OCT catheter was developed for estimating the volume of the accessible workspace. Experimental validation was done using electromagnetic tracking of the catheter's positions. An exemplary scanning path was then selected within the available workspace to evaluate motion performance with the robotized steerable OCT catheter. Automatic scanning is compared to a teleoperated one and a manual scanning with a nonrobotized flexible endoscope. Spectral arc length, scanning area, spacing between scan trajectories, and time are metrics used to quantify performance.

**Results:** The available scanning workspace was experimentally estimated to be 255 cm<sup>3</sup>. The automatic scanning mode provided the highest accuracy and smoothness of motion with spectral arc length of -3.18, covered area of 10.11 cm<sup>2</sup>, 1.54 mm spacing between 15 sweep trajectories, maximum translation of 27.99 mm, and time to finish of 3.11s.

**Conclusions:** Automatic modality improved the accuracy of scanning within a large workspace. The robotic capability provided better control to the user to define spacing resolution of scanning patterns.

© The Authors. Published by SPIE under a Creative Commons Attribution 4.0 International License. Distribution or reproduction of this work in whole or in part requires full attribution of the original publication, including its DOI. [DOI: [10.1117/1.JOM.3.1.011005](https://doi.org/10.1117/1.JOM.3.1.011005)]

**Keywords:** optical coherence tomography; endoscopy; gastroenterology; robot-assisted surgery; steerable devices; workspace.

Paper 22016SS received Jul. 1, 2022; accepted for publication Jan. 3, 2023; published online Jan. 19, 2023.

\*Address all correspondence to Michalina J. Gora, [gora@unistra.fr](mailto:gora@unistra.fr)

## 1 Introduction

Optical coherence tomography (OCT) is an imaging technology that has been widely developed primarily for ophthalmology.<sup>1</sup> To achieve volumetric images of the retina, external galvo mirrors are implemented to scan a near-infrared light over the posterior part of the human eye in a non-contact way.<sup>2</sup> The obtained detailed information about the structure of the eye in healthy and diseased conditions enabled new treatment approaches that required extreme precision of gestures.<sup>3</sup> This motivated the first work combining robotics and OCT to assist in ophthalmic procedures and to improve image acquisition through stabilization of the OCT probe with respect to the target.<sup>4</sup> Similar to ophthalmology, the vast majority of prior work in the use of OCT in the digestive system was focused on improving the diagnosis of digestive diseases.<sup>5</sup> The advancement of new imaging methods enabled early diagnosis, which in turn allowed minimally invasive treatment with flexible endoscopes in the gut.

Endoscopic OCT catheters are conventionally inserted into the digestive system using a working channel of a white light (WL) endoscope.<sup>6-11</sup> To obtain OCT volumetric information, the side-focused optical probe inside of a static sheath is rotated and pulled back. The sheath can have a form of a balloon, a low-profile tube, or a capsule.<sup>12-14</sup> The working distance is typically located few hundred micrometers outside of the sheath. A cylindrical area defined by the length of the pullback stroke and the working distance of the optics defines the optical scanning area. Endoscopic OCT with balloon catheters was commercialized for imaging of a distal section of the esophagus where Barrett's esophagus is typically located.<sup>15</sup> In this design, a scanning area ranges from 26.38 to 37.7 cm<sup>2</sup>, considering 6 cm pullback and balloon diameters between 14 and 20 mm.<sup>16</sup> The scanning range of low-profile catheters, on the other hand, is much smaller, with a coverage area of 4.40 cm<sup>2</sup> for an outer diameter of 2.33 mm and pullback length of 6 cm.<sup>16</sup> Thus the endoscope and WL images have to be used to position the OCT probe in the area of suspicious lesions. Tethered capsule endomicroscopy (TCE) does not require an endoscope for insertions, and it provides the largest coverage area of 60 cm<sup>2</sup> with an outer diameter of 12.8 mm and 15 cm of manual pullback length.<sup>14</sup>

With low-profile and balloon catheters, examination of larger sections of the internal organs can be obtained by repositioning the probe, which still presents several challenges. The balloon OCT catheters can be deflated, advanced in the esophagus, and inflated again but it does not allow for insertion of any other tools and it blocks WL camera view during examination. Low-profile catheters do not interfere with the endoscopic camera view, and the endoscope can be used to manually move the probe over the tissue for scanning. However, such manual scanning will cause the endoscope head to move, which can be a problem for visualization during endoscopic treatment procedures. TCE does not require an endoscope for insertion but its displacement highly depends on the action of swallowing by the patient, peristalsis, and manual pulling of the tether. It is also expected that manual scanning will have limited capabilities, especially in terms of sampling uniformity. As an example, a manual pullback in TCE was not sufficient for en-face reconstruction, and a short inner pullback was proposed to overcome this problem.<sup>17</sup>

Correct sampling is crucial in any medical imaging technology for optimal image reconstruction and visualization.<sup>18,19</sup> As OCT collects a one-dimensional information in a single measurement, scanning is needed for obtaining volumetric information. In comparison to ophthalmic imaging, endoscopic OCT requires miniature scanning mechanisms. Depending on the design, various scanning patterns can be found in the literature, such as raster, circular, spiral, and Lissajous scanning.<sup>20-25</sup> In order to achieve such microscan patterns, micromirrors have been implemented with microelectromechanical systems (MEMS) based on electrostatic,<sup>24,25</sup> electromagnetic (EM),<sup>26</sup> and electrothermal actuation,<sup>27,28</sup> as well as actuation of lensed fibers using piezoelectric devices,<sup>29,30</sup> micromotor,<sup>31</sup> and proximal actuated fiber optic rotary joints.<sup>32</sup> Various side-viewing and forward-viewing designs of endoscopic probes have been demonstrated in the literature.<sup>5,33</sup> The field of view provided by microscanners is limited to a few millimeters due to the miniaturization requirements to fit the probes into endoscopic channels, typical outer diameters of 2.8 mm are used in gastroscopes.<sup>5</sup> OCT probes have also been implemented in smaller devices such as needles with diameters under 1 mm.<sup>34</sup> When imaging larger areas is required, as in the case of the digestive system, the limited field-of-view forces the operator to manually move the probe to reach nonvisible areas so that precisely controlling the motion

of the probe from a long distance is difficult due to lack of fine control and lack of 3D perception. Moreover, friction in the mechanisms hinders scanning uniformity, resulting in an irregular pattern. Similar problems are also typical for other microscopic techniques, like probe-based confocal endomicroscopy (pCLE). Zhang et al. integrated pCLE and OCT for control of the da Vinci surgical robot and performed extended field-of-view image scans with both optical technologies during laparoscopic procedures.<sup>35</sup> Giataganas et al.<sup>36</sup> described a robotic scanner capable of performing programmed trajectories exceeding pCLE field of view and achieving 3 mm<sup>2</sup> of scanning area for breast tissue. Giataganas et al.<sup>37</sup> also proposed a force-controlled pick-up probe for integration with the robotized da Vinci instruments in intraoperative endomicroscopy imaging. The device is intended to maintain constant contact between the porcine colon tissue and the imaging probe, improving optical scans over large and complex surfaces. Draelos et al.<sup>38</sup> reported the implementation of a robotized OCT probe to align and stabilize OCT image acquisitions of a moving target for ophthalmology.

Image stitching techniques have been proposed to reconstruct the imaging area of an extended field of view.<sup>39–43</sup> As an example, Lurie et al.<sup>30</sup> demonstrated expanding the field of view of a scanning forward-viewing endoscopic OCT catheter from 0.95 mm<sup>2</sup> spiral pattern to cover an area of 19 mm × 10.4 mm intended for cystoscopy. The extended field of view was achieved by stitching images obtained after manual repositioning of the probe. To extend the field of view of endoscopic micro-optical imaging devices, automatic scanning systems have also been proposed. For instance, Rosa et al.<sup>44</sup> developed a robotic imaging system to increase the field of view of a probe-based confocal laser endomicroscopy from 200 μm × 240 μm diameter to 1700 μm × 1700 μm by performing automatic raster scanning over *ex vivo* abdominal tissue.

The aforementioned solutions to extend the field of view of optical imaging benefit from the robotic systems developed to decrease complexity of minimally invasive surgical procedures. One such system is a robotized flexible endoscope designed for minimally invasive endoscopic treatment by endoscopic submucosal dissection of an early-stage colorectal cancer.<sup>45</sup> This robotized system, however, relies only on WL camera imaging to find and delineate the lesion. OCT has the potential of providing *in situ* optical biopsy, but considering that the diameter of the colon can be up to 9 cm in the cecum<sup>46</sup> extended field of view is crucial to assist during the procedure.

Here we propose an automatic scanning with a steerable OCT catheter to improve imaging performance while scanning areas larger than the field of view of a low-profile OCT probe. The device implements custom endoscopic OCT system with proximal rotational scanning for imaging in gastrointestinal applications. First, we formulate a geometrical model of the steerable OCT catheter that we use for the estimation of the volume of the accessible optical scanning region, which corresponds to the steerable catheter workspace. The model is based on previously published modeling of active catheters,<sup>47</sup> a common concept in robotics and being adapted here for optically imaging catheters. The OCT imaging workspace that can be achieved thanks to three degrees of freedom (DoF) is a volumetric region validated experimentally using an EM tracking of the catheter's position. We select from the available workspace a scanning path designed for examination of lesion margins with the robotized flexible endoscope and the steerable OCT catheter. We compare the trajectory performance obtained in the automatic mode to the performance obtained by a trained user operating the device in the teleoperation mode. We also compare it with the performance using a conventional manual endoscope equipped with a nonsteerable low-profile OCT catheter. To analyze the performance of different scanning settings we propose to use the spectral arc length as a quantitative metric for smoothness of motion. This metric measures the arc length of the Fourier magnitude spectrum of the speed profile of a robotic tool. Spectral arc length quantifies smoothness of motion and it is independent of the amplitude, duration, and trajectory. It has been previously demonstrated to be robust and consistent for analysis of smoothness of motions in sport science, psychology, and neuro-rehabilitation,<sup>48</sup> as well as for skills analysis in surgery<sup>49</sup> and assessment of performance in robotic systems.<sup>50,51</sup> The smoothness of motion is an indicator of the distribution uniformity of data acquisition. Scan area, spacing, number of sweep trajectories achieved, translation, and time to finish are also considered in this work to measure scanning performance.

## 2 Methods

### 2.1 Workspace Model

The workspace of a robotic system is defined by Waldron and Schmedeler as “the total volume swept out by the end-effector of a robotic manipulator as it executes all possible motions.”<sup>52</sup> The end-effector in the steerable OCT catheter corresponds to the focusing optics at the distal end of the probe. In this paper, we call scanning workspace the total volume that can be reached by the robotic OCT manipulator as all DoFs sweep their complete stroke with respect to the output of the instrument channel. The steerable OCT device is an active catheter of piecewise constant curvature<sup>53</sup> that consists of 11 links in the distal end<sup>54</sup> driven by two antagonist cables (Fig. 1). The position of the OCT imaging probe depends on a bending section of length  $L$  that can be bent by an angle  $\beta$  in a plane, whose orientation can be defined by rotation  $\phi$ . Moreover, the tool can be translated by a quantity  $\Delta T$  in the bending plane. The radius of curvature of the bending section is denoted as  $R$  with  $L = R\beta$ .

The position of the focusing optics is separated from the distal end of the bending section by a rigid part with length  $I$ . This distance can be varied by an internal translation of the probe that pulls back the focusing optics ( $\Delta I$ ) placed inside the static outer sheath. The position of the focusing optics in the rigid section is then given by  $I = I_0 + I_{\max} + \Delta I$ . The four variable parameters have the following ranges:  $\beta = [-90, 90]$  deg,  $\phi = [0, 360]$  deg,  $\Delta T = [-T_{\max}, 0]$  mm, and  $\Delta I = [-I_{\max}, 0]$  mm.

The position of the tool’s tip with respect to the base of the bending section is given by Eqs. (1) and (2) in terms of the bending angle, whereas Eq. (3) sets the  $y$ -coordinate of the tool’s tip in the bending plane with respect to the endoscopic channel illustrated in Fig. 1. Deduction of Eqs. (1) and (2) is based on the work of Jones et al.<sup>47,53</sup>

$$x_I = \frac{2L}{\beta} \left( \sin\left(\frac{\beta}{2}\right) \right)^2 + I \sin(\beta), \quad (1)$$

$$y_I = \frac{L}{\beta} \sin(\beta) + I \cos(\beta), \quad (2)$$

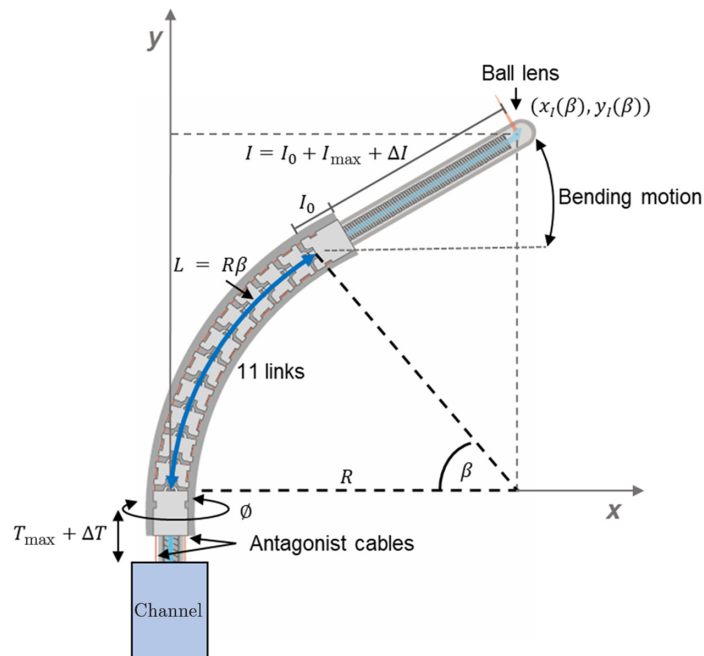


**Fig. 1** Distal end of the steerable OCT catheter of piecewise constant curvature. It consists of a bending section of length  $L$  made of 11 links and a rigid segment of length  $I$ .

$$y_I^* = y_I + T_{\max} + \Delta T. \quad (3)$$

In the case when the tool is straight ( $\beta = 0$ ) with no retraction translation ( $\Delta T = 0$ ), then  $x_I = 0$  and  $y_I^* = L + I + T_{\max}$ .

Figure 2(a) shows a cross-sectional view of the workspace described by Eqs. (1)–(3). The steerable OCT tool is shown in three limit positions: straight with no translation (most extended) of the tool (red), maximum bending with no translation (yellow), and maximum bending with maximum translation, i.e., most retracted (blue).

The contour of the workspace in the bending plane can be decomposed into the following paths (Table 1) that are presented as a function of the DoF  $P(\Delta T, \beta, \Delta I, \phi)$ :

- $P_0 = P(0, 0 \text{ deg}, 0, 0 \text{ deg})$  is the position when the tool is straight and fully extended out of the endoscopic channel.
- $P_A = P(0, -90 \text{ deg} \leq \beta \leq 0 \text{ deg}, 0, 0 \text{ deg})$  is the path achieved by bending from 0 deg to  $-90$  deg, and no retraction translation, pullback, or rotation.
- $P_B = P(-T_{\max} \leq \Delta T \leq 0, -90 \text{ deg}, 0, 0 \text{ deg})$  is the path achieved by translating from 0 to  $-T_{\max}$  while keeping the bending at  $\beta = -90$  deg, and no pullback of the OCT probe or rotation of the tool.

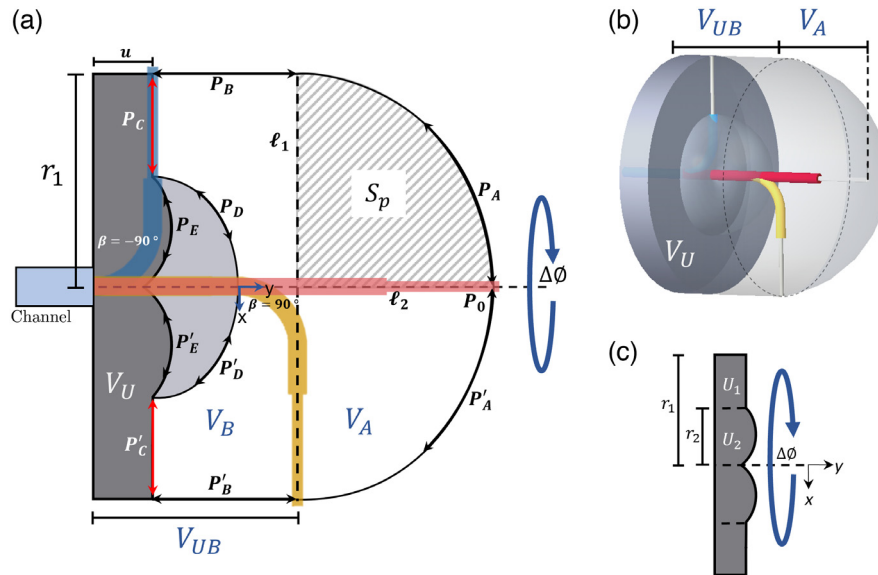


**Fig. 2** (a) 2D view of the workspace model of the steerable OCT catheter. The figure shows three limits configurations: the straight position, maximum bending at 90 deg and at maximum translation–maximum bending at  $-90$  deg. (b) 3D representation of the workspace. (c) 2D view of the unreachable workspace.

**Table 1** Path of the probe tip as a function of the DoF while keeping  $\phi = 0$ .

Path	$\Delta T$ (mm)	$\beta$ (deg)	$\Delta I$ (mm)
$P_A$	0	$-90 \leq \beta \leq 0$	0
$P_B$	$-T_{\max} \leq \Delta T \leq 0$	$-90$	0
$P_C$	$-T_{\max}$	$-90$	$-I_{\max} \leq \Delta I \leq 0$
$P_D$	$-T_{\max}$	$-90 \leq \beta \leq 0$	$-I_{\max}$
$P_E$	$< -T_{\max}$	$-90 \leq \beta \leq 0$	$-I_{\max}$

- $P_C = P(-T_{\max}, -90 \text{ deg}, -I_{\max} \leq \Delta I \leq 0, 0 \text{ deg})$  is the path achieved by pulling back the OCT probe from 0 to  $-I_{\max}$  while keeping the tool at  $\Delta T = -T_{\max}$ ,  $\beta = -90 \text{ deg}$ , and no rotation.
- $P_D = P(-T_{\max}, -90 \text{ deg} \leq \beta \leq 0 \text{ deg}, -I_{\max}, 0 \text{ deg})$  is the path achieved by bending the angle  $\beta$  from  $-90 \text{ deg}$  to  $0 \text{ deg}$  while keeping retraction translation at  $\Delta T = -T_{\max}$ , OCT probe pullback at  $\Delta I = -I_{\max}$  and no rotation of the tool.
- $P_E = P(\Delta T < -T_{\max}, -90 \text{ deg} \leq \beta \leq 0 \text{ deg}, -I_{\max}, 0 \text{ deg})$  corresponds to the case where the tool is fully retracted into the endoscopic channel, this path is achieved by performing a synchronized motion between retraction translation of the tool beyond maximum translation  $-T_{\max}$  for  $\Delta T < -T_{\max}$  and bending  $\beta$  from  $-90 \text{ deg}$  to  $0 \text{ deg}$ , whereas keeping the OCT probe pullback in  $\Delta I = -I_{\max}$  in the bending plane  $\phi = 0 \text{ deg}$ .

The tip of the tool can be positioned at any place enclosed into the limiting regions in Fig. 2(a), where there is no kinematic singularity within the motion ranges of the actuators, thus the entire workspace can be covered. A proof of no singularity can be found in chapter 8 in the Elsevier Handbook of Robotic and Image-Guided Surgery.<sup>55</sup> The dark gray color region in Figs. 2(a) and 2(b) represents the region that is not reachable by the tip of the tool.

The  $y$ -axis distance that separates the endoscopic channel and the tip of the instrument in  $P_C$  is indicated as  $u$ , it delimits the unreachable workspace and also corresponds to the radius of the bending section of the tool when  $\beta = \pm 90 \text{ deg}$ . A 3D model of the envelope of the workspace shown in Fig. 2(b) is obtained by varying the rotation angle of the tool  $\phi = [0 \text{ deg}, 360 \text{ deg}]$  for every path case of the upper half of the plane above the central axis  $\ell_2$ , this axis is parallel to the extended straight position of the tool described in Fig. 2(a) and Table 1. The paths denoted by  $P'_{(A,B,C,D,E)}$  correspond to the mirror positions of the tool with positive values of  $\beta$ .

The volume covered by the full rotation of the surface  $S_p$  delimited by  $P_A$ , the axis  $\ell_1$  perpendicular to  $\ell_2$  (dashed lines) and  $\ell_2$  is denoted by  $V_A$ , whereas  $V_B$  refers to the volume spanned by rotation of the surface covered by paths  $P_B, P_C, P_E$  and axis  $\ell_1, \ell_2$ .  $V_U$  corresponds to the volume of the unreachable workspace in dark gray color.  $V_{UB}$  is the union of volumes  $V_U \cup V_B$ .

The volume of the workspace covered by the robotized OCT device is given by Eq. (4), where  $V_T$  refers to the total volume and is composed by the addition of  $V_A$  and the cylindrical volume  $V_{UB}$  and the subtraction of the volume of the unreachable workspace  $V_U$  as illustrated in Fig. 2(a)

$$V_T = (V_A \cup V_{UB}) - V_U. \quad (4)$$

The volume  $V_A$  is delimited by the hatched area  $S_p$  in Fig. 2(a), for which the bending angle is actuated for the range  $\beta = [-90 \text{ deg}, 0]$ , and by the full range rotation  $\phi = [0^\circ, 360^\circ]$ , whereas there is no retraction translation ( $\Delta T = 0$ ) and no OCT probe pullback ( $\Delta I = 0$ ). Therefore, based on the theorem of Pappus for volumes of revolution,<sup>56</sup> the volume  $V_A$  can be computed by taking the area  $S_p$  defined in Eq. (5) and performing full rotation about the  $y$ -axis [Eq. (6)] following a circumference defined by  $2\pi\bar{x}$ , where  $\bar{x}$  refers to the arithmetic mean of the positions of the hatched area along the  $x$  axis

$$S_p = \int_{-\pi/2}^0 (y_I(\beta) - u)x'_I(\beta)d\beta, \quad (5)$$

$$V_A = 2\pi\bar{x}S_p. \quad (6)$$

In Eq. (5),  $u$  has been subtracted from  $y_I(\beta)$  to compute  $S_p$ , this is based on Fig. 1 where  $y_I(\beta)$  represents the  $y$  component of the position of the tip, whereas  $x'_I(\beta)$  the derivative of the  $x$  component in parametric format. Figure 2 shows the position of the  $x$ - $y$  base frame related to Fig. 1. Computation of  $\bar{x}$  is defined by Eq. (7) and its demonstration can be found in a general calculus book, for this article we based our computation on the book Calculus 10th edition, page 395 by

Anton and Davis.<sup>56</sup> Positive values of bending angle  $\beta$  are used for simplicity in the integration limits, as this will not affect the result.

$$\bar{x} = \frac{\int_0^{\pi/2} x_I(\beta)(y_I(\beta) - u)x_I'(\beta)d\beta}{\int_0^{\pi/2} (y_I(\beta) - u)x_I'(\beta)d\beta}. \quad (7)$$

The volume  $V_{UB}$  is delimited by the cylindrical region formed by the surface enclosed into  $r_1$ ,  $u$ ,  $P_B$ ,  $\ell_1$ ,  $\ell_2$  [Fig. 2(a)] and spanning the full rotation angle  $\phi = [0 \text{ deg}, 360 \text{ deg}]$  with the tool about  $\ell_2$ .  $V_{UB}$  is defined in Eq. (8) as

$$V_{UB} = \pi r_1^2 (T_{\max} + |u|). \quad (8)$$

The unreachable workspace  $V_U$  is composed by the volume of the regions  $U_1$  and  $U_2$  in Fig. 2(c). The volume  $V_{U_1}$  is described by a ring geometry as

$$V_{U_1} = \pi(r_1^2 - r_2^2)u. \quad (9)$$

The volume  $V_{U_2}$  is computed with the theorem of Pappus for volumes of revolution, taking the area of the region  $U_2$  and performing a revolution around the  $y$  axis. The radius  $R$  is kept constant to  $R = L/(\pi/2)$ , and  $\Delta I = -I_{\max}$  in Eqs. (1) and (2) with  $-90 \leq \beta \leq 0$ . Then the computation procedure is the same as for  $V_A$ : computing the centroid  $\bar{x}$  using Eq. (7) with  $u = 0$  rewritten in Eq. (10), then computation of volume  $V_{U_2}$  with Eq. (6). The volume of the unreachable workspace is given by Eq. (11)

$$\bar{x} = \frac{\int_0^{\pi/2} x_I(\beta)(y_I(\beta))x_I'(\beta)d\beta}{\int_0^{\pi/2} (y_I(\beta))x_I'(\beta)d\beta}, \quad (10)$$

$$V_U = V_{U_1} + V_{U_2}. \quad (11)$$

Finally, the total volume of the workspace is computed by adding  $V_A$  to  $V_{UB}$  and subtracting  $V_U$  as expressed in Eq. (4).

## 2.2 Experimental Workspace Validation

The experimental validation of the workspace was achieved using the Aurora EM tracker from NDI Digital, Inc. and two sensor coils (610060). One sensor was positioned at the tip of the OCT catheter, which matches the position of the optical probe at  $\Delta I = 0$ , and the other one was placed at the exit of the endoscope channel [Fig. 3(a)]. This sensing configuration allows for the collection of the optical probe positions with respect to the output of the instrument channel while performing motion patterns for the three DoFs of the tool: bending, rotation, and translation. The sampling rate of the EM tracker was 40 samples per second. The experimental set-up is shown in Fig. 3(b) with the steerable OCT tool set to a maximum bending of 90 deg.

## 2.3 Automatic Scanning Strategy

One of the advantages of the robotic OCT catheter is the capability of implementing programmed trajectories preoperatively defined by the user, which can then be performed automatically under the supervision of the user. To assess this point, we proposed an experiment where the steerable OCT catheter will automatically follow a given reference trajectory. We compare the automatic scanning to a scanning effectuated under direct user control using a teleoperated robot, and manually using a conventional endoscope (Fig. 4). The proposed experiment requires three elements described below: a reference trajectory to be followed, performance metrics for evaluation, and a dedicated experimental setup.

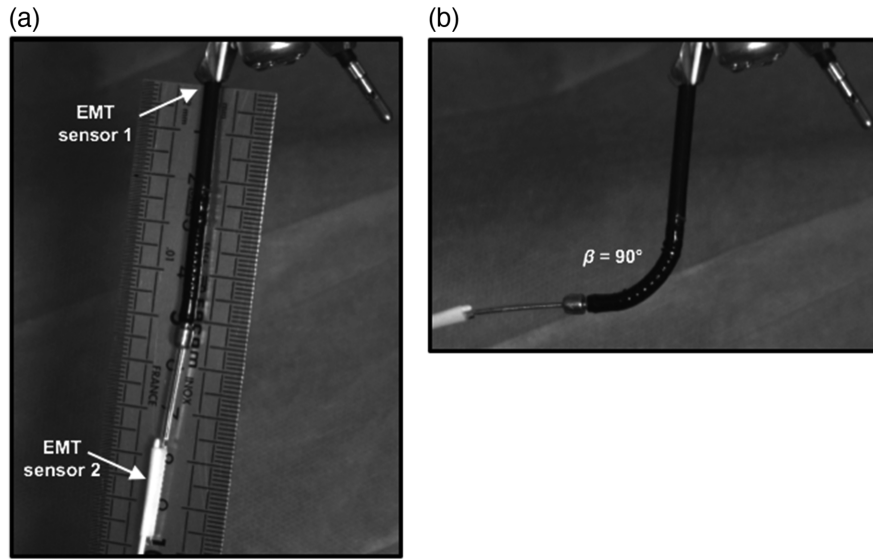


**Fig. 3** (a) Picture of the distal end of the robotized interventional endoscope with the steerable OCT catheter, the tool is in a straight position with marked location of two sensors of the EM tracker. (b) The steerable OCT catheter in 90 deg bending angle configuration.

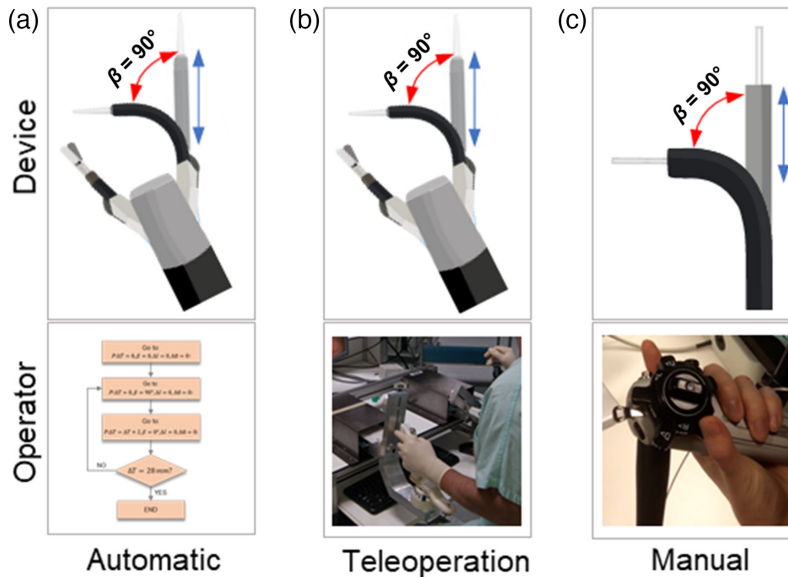


**Fig. 4** Schematic drawing of the distal tip of the endoscopic system with inserted OCT probe (top row) and operation type (bottom row) for (a) automatic, (b) teleoperation, and (c) manual configuration.

### 2.3.1 Reference trajectory

The reference trajectory was designed in order to allow scanning a given area and detect small lesions. It is shown in Fig. 5(a). The reference path is composed of 15 repetitions of an elementary back-and-forth sweeping, with a spacing of 2 mm in translation, therefore covering a total distance of 28 mm. Note that during this motion of the tool, the OCT probe implements rotational scanning to constantly acquire OCT frames. The elementary movement consists of the bending motion of the OCT tool from the straight position to a maximum bending angle of 90 deg (later referenced as a *sweep*), then returning back to the straight position while performing synchronized translation of the tool by  $\Delta T = -2$  mm, the negative value indicating retraction

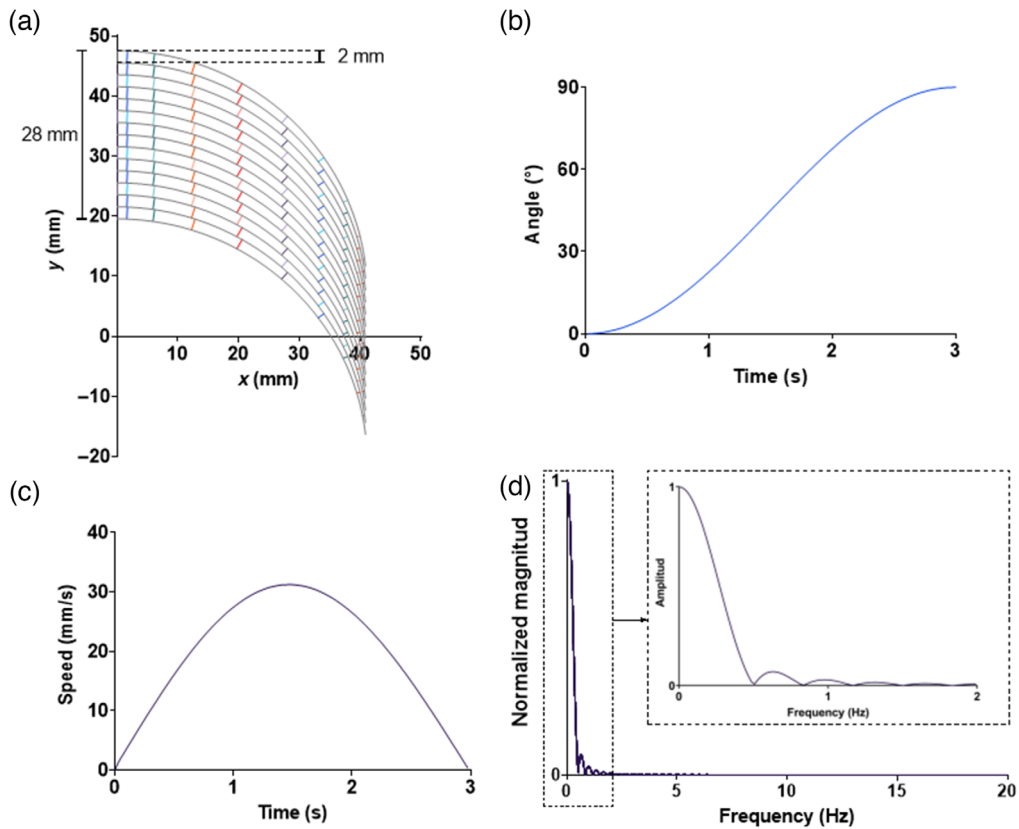


**Fig. 5** (a) Spatial reference trajectory with bending angle from 0 deg to 90 deg, translation of 28 mm and spacing of 2 mm. (b) Sinusoidal evolution of the bending angle for one sweep. (c) Expected speed profile for each sweep trajectory of the probe tip. (d) Spectrum of the speed profile.

direction.  $\Delta T$  was chosen so that the spacing between lines can be seen by the user on the WL images in manual and teleoperated modes.

The speed of the reference trajectory is set so that a sweep is performed in 3s, which allows recording sufficient datapoints for assessing the trajectory with the EM sensor on the tooltip, whereas being possible to perform in the three control modes. It is, however, not constant. Indeed, achieving a high smoothness of the scanning speed is important to avoid abrupt speed scanning changes resulting in an irregular spatial sampling. We chose a sinusoidal variation of the bending angle from 0 deg to 90 deg for tissue scanning [Fig. 5(b)] as reference for maximum smoothness. Figure 5(c) shows the expected speed profile for one sweep.

### 2.3.2 Evaluation metrics

To compare the automatic scanning to the teleoperated and manual modes, we use the mean spacing between sweeps  $s$ , the number of performed sweeps  $s_w$ , the coverage area  $A$ , the time per sweep  $t$ , and the spectral arc length  $\eta_{SAL}$ .

To calculate the spacing between actual sweep paths  $s$ , first a curve was fitted to each sweep path recorded using the EM tracker to have a uniform spatial sampling of each path. Then the smallest distance to the adjacent curve was found for points sampled on the path. The mean value  $s$  of the spacing was computed for 11 points between each pair of curve paths. The same data was used to compute the number of sweeps actually performed  $s_w$ , (which can vary especially in the teleoperation and manual modes), as well as the average time  $t$ . The coverage area  $A$  was computed by subtracting the area resulting of integrating the curve represented by the higher positions from the curve with lower positions in Fig. 5(a).

Smoothness of motion is an important element when considering micro-probe scanning. This was quantified using the spectral arc length metric that measures the shape of the spectrum signal of the speed profile in a given movement, and it is independent of its amplitude and duration. It was previously introduced by Balasubramanian et al.<sup>48</sup> and defined in Eq. (12) for a given movement.  $\omega_c$  corresponds to the frequency band occupied by the movement,  $V(\omega)$  is the Fourier magnitude spectrum of the speed profile, and  $\hat{V}(\omega)$  is the amplitude normalized magnitude spectrum. This metric has been used to measure motor recovery in patients affected by neurological diseases, and also for quantifying robotic catheter performance<sup>50,51</sup>

$$\eta = - \int_0^{\omega_c} \sqrt{\left(\frac{1}{\omega_c}\right)^2 + \left(\frac{d\hat{V}(\omega)}{d\omega}\right)^2} d\omega \quad \hat{V}(\omega) = \frac{V(\omega)}{V(0)}. \quad (12)$$

To assess movement smoothness during the whole trajectory, but without undue influence of abrupt trajectory changes at the beginning and end of each sweep, we compute the value of  $\eta$  for each single sweep trajectory. The average spectral arc length for each sweep, was then computed using Eq. (13) and reported as the average smoothness of motion performed during the whole scanning trajectory

$$\eta_{\text{SAL}} = \frac{1}{s_w} \sum_{i=1}^{s_w} \eta(i), \quad (13)$$

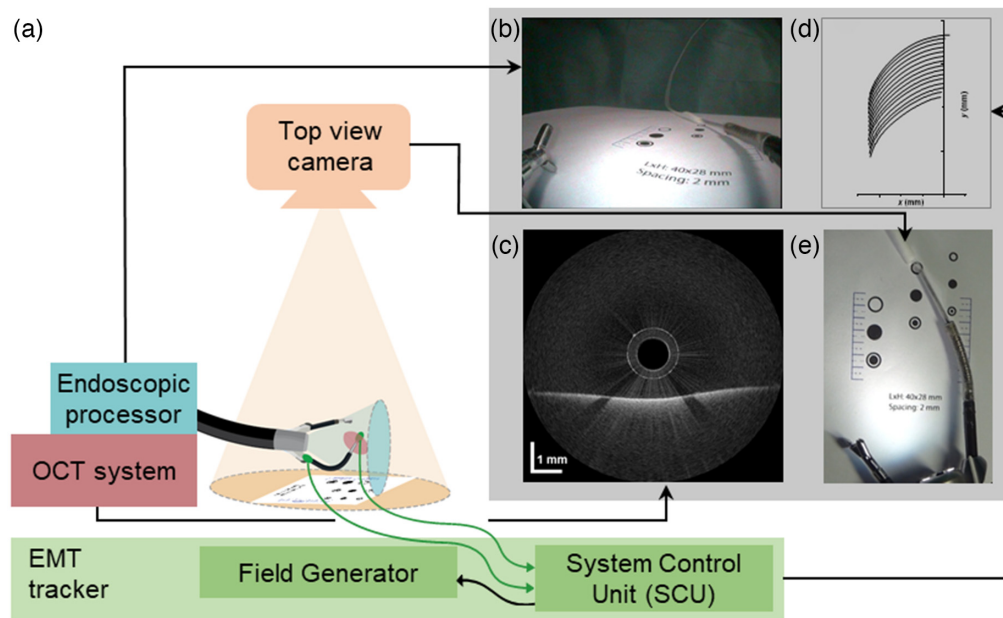
where  $\eta(i)$  is the spectral arc length for a given sweep  $i$ .

Figure 5(d) shows the expected Fourier transform for the speed profile in Fig. 5(c) corresponding to the one sweep reference trajectory in Fig. 5(a). A motion with lower smoothness will add extra components to the spectrum, resulting in a longer spectral arc length, so that a value closer to zero means higher smoothness of the motion. The theoretical highest value of  $\eta_{\text{SAL}}$  was computed as  $-2.17$  with Eq. (12), then using Eq. (13) to calculate the average of the spectral arc lengths of all spectra corresponding to the reference sweep trajectories in Fig. 5(a), the speed profile spectrum for one sweep trajectory is represented in Fig. 5(d). A spectral bandwidth of 20 Hz was used because the sampling frequency of the EM tracker is 40 Hz.

## 2.4 Experimental Setup for Testing Scanning Trajectories

The reference trajectory described in Fig. 5 has been experimentally effectuated in the automatic mode and compared to teleoperation and manual scanning (Fig. 6). Both the automatic and teleoperated trajectories were performed with a robotized flexible endoscope, based on an interventional endoscope from Karl Storz. The steerable OCT catheter was inserted through one of the two instrument channels. In the automatic mode, the predefined trajectory was scanned automatically without any user intervention. In the teleoperation mode, the user manipulated the OCT catheter using a remote master controller. The performance of the automatic and teleoperated OCT scanning was compared to scanning achieved with a standard of care manual endoscope (13821 PKS, Karl Storz) with a low-profile side-viewing OCT catheter that was inserted through the working channel. The endoscope was operated by an expert gastroenterologist. The same optical core with a proximal actuation was used with both manual and robotized endoscopes and cross-sectional OCT images were collected using an Axsun-based OCT system operating at 1300 nm.

In all modes, WL endoscopy video [Fig. 6(b)] and radial OCT images [Fig. 6(c)] were available to the operators to follow the trajectory. The OCT probe was scanned over a printed target [Figs. 6(b) and 6(e)] with millimeter side frames that could be used by operators as guides to reproduce the reference scanning pattern. The circular ink printed features with different characteristics were added to the target to assure that recognizable OCT data was obtained. In addition, in all experiments the EM tracker data [Fig. 6(d)] were collected for a quantitative comparison of the spatial positions of the probe and an external top view camera was used for recording the motion of instruments [Fig. 6(e)].



**Fig. 6** (a) Experimental setup with (b) endoscopic view showing the EM tracker sensor, the OCT probe, and the printed target features. (c) The OCT image view of the printed 4 mm ring-like feature. (d) The collected trajectory data from the EMT tracker. (e) External top view of the robotized endoscope, the steerable OCT catheter, and printed target features. The EM tracker is composed by the system control unit (SCU), the magnetic field generator and two sensors connected to the tip of the optical device and output of the surgical channel.

### 3 Results

#### 3.1 Experimental Workspace Validation

To measure the total accessible volume of the steerable OCT catheter delimited by the regions described in Figs. 2(a) and 2(b), the robotized steerable OCT device was programmed to automatically follow trajectories of sequential bending, translation, and rotation. The trajectories were programmed to place the tip of the probe at different positions enclosed in the volumetric regions described by the geometrical model in Figs. 1 and 2. The sweep pattern in one plane was performed by step 1: applying full bending of the catheter, step 2: translating it in 3 mm steps between each sweep over the actual limit length of 29.7 mm; the greater translation was achieved due to space between the inner diameter of the instrument channel and the outer diameter of the tool [Fig. 7(a)]. The achieved bending range was from  $-60$  deg to  $90$  deg. The incomplete bending in one direction was caused by asymmetry of the configuration of end stops on the cable driving system controlling bending. In the next step 3: the orientation of the steerable OCT catheter was rotated until the full turn ( $\Delta\phi = 360$  deg) was achieved. Figure 7(b) shows the rotational trajectory of the steerable tool for a bending angle of  $90$  deg. The maximum rotation of the tool achieved in one direction was  $353.08$  deg. It is important to mention that the OCT tool can be rotated in both directions to reach  $360$  deg of rotation. The sweep pattern repeated in steps of  $\Delta\phi = 36$  deg representing 10 angular positions until completing  $\Delta\phi = 360$  deg was used to employ the three available DoF of the OCT catheter to test the available scanning volume [Fig. 7(c)]. The point cloud data collected from EM tracker was processed and analyzed by computation of the convex hull of the points set using MeshLab [Fig. 7(d)].<sup>57,58</sup> The estimated volume was  $255$  cm<sup>3</sup>, which corresponds well to the volume of  $263$  cm<sup>3</sup> calculated based on the real dimensions of the tool and the model described in Sec. 2.1.

#### 3.2 Automatic Scanning Trajectory

To test a predefined automatic scanning and compare it to teleoperation and manual modes the printed scanning target was placed in a closed box to assure that the operators would be using

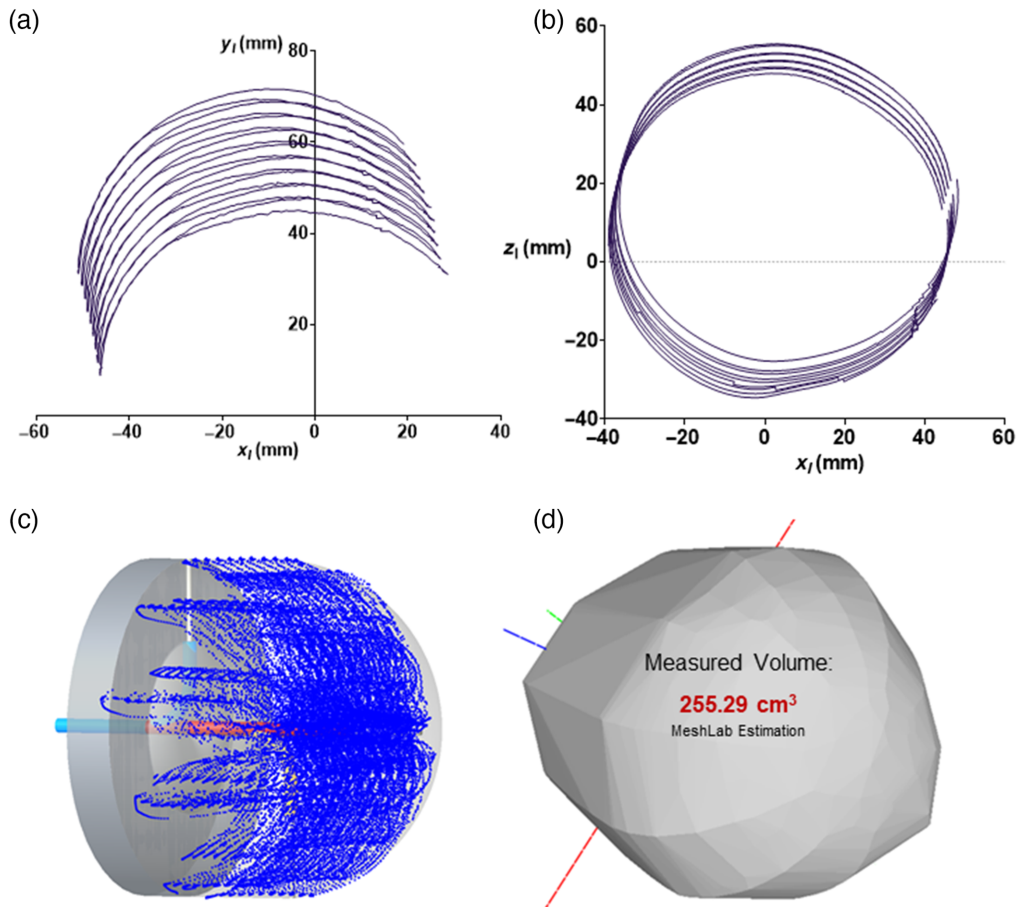
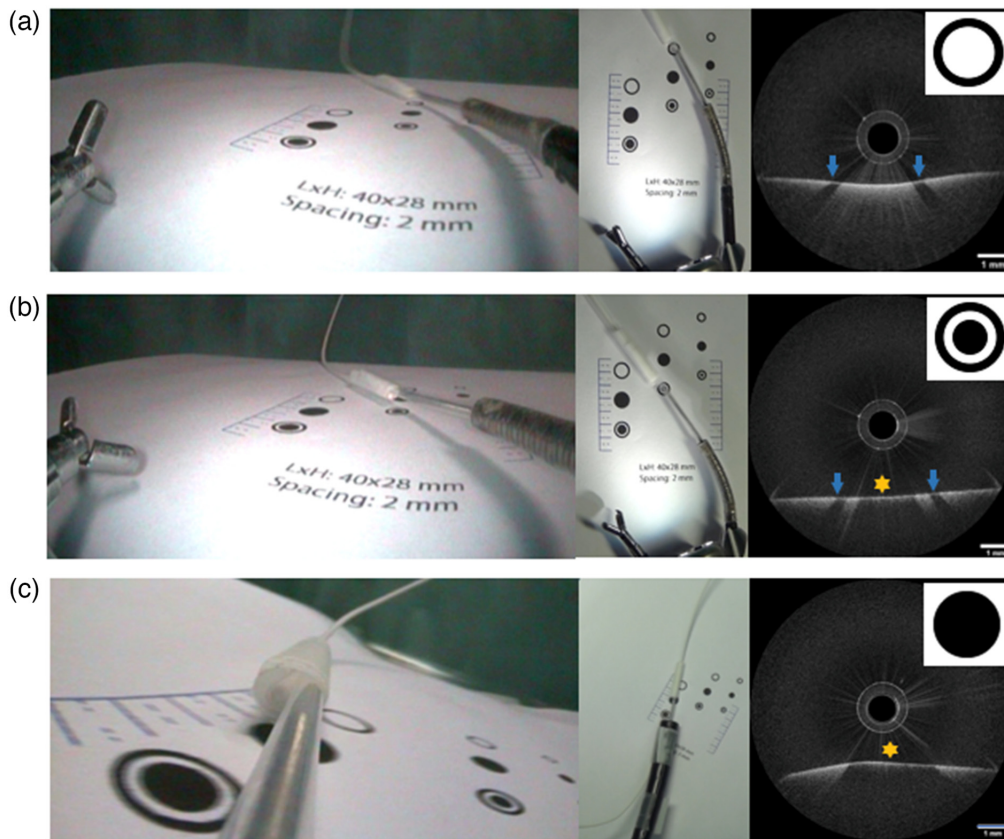


**Fig. 7** Point cloud data obtained from EM tracker during: (a) sweeping pattern with full catheter bending in both directions and translation, (b) rotation pattern with translation, (c) combined bending, translation and rotation pattern covering the full available workspace. (d) Volume estimation of the convex hull with MeshLab.

WL endoscopy video for orientation (left column in Fig. 8) and OCT real-time images (right column in Fig. 8) to assure good quality of the data. In addition, in all three configurations (automatic, teleoperation, and manual), a top view camera was used to confirm the tip position in post-processing (Fig. 8), but this visualization was not available for the user during the scanning tasks. In the OCT cross-sections, three different circular features from the printed target can be seen. Figure 8(a) shows a cross-sectional image of a black ink ring, the black borders of the circle can be clearly visualized thanks to a high absorption of the ink (see arrow marks in image). Figure 8(b) shows another feature composed of a full black ink circle (see star mark in the image) surrounded by a black ring outer circle imaged. In Fig. 8(c), a full filled black ink circle is visualized in the OCT image, obtained during the manual scanning test. The features were useful for scanning and position guidance of the OCT device.

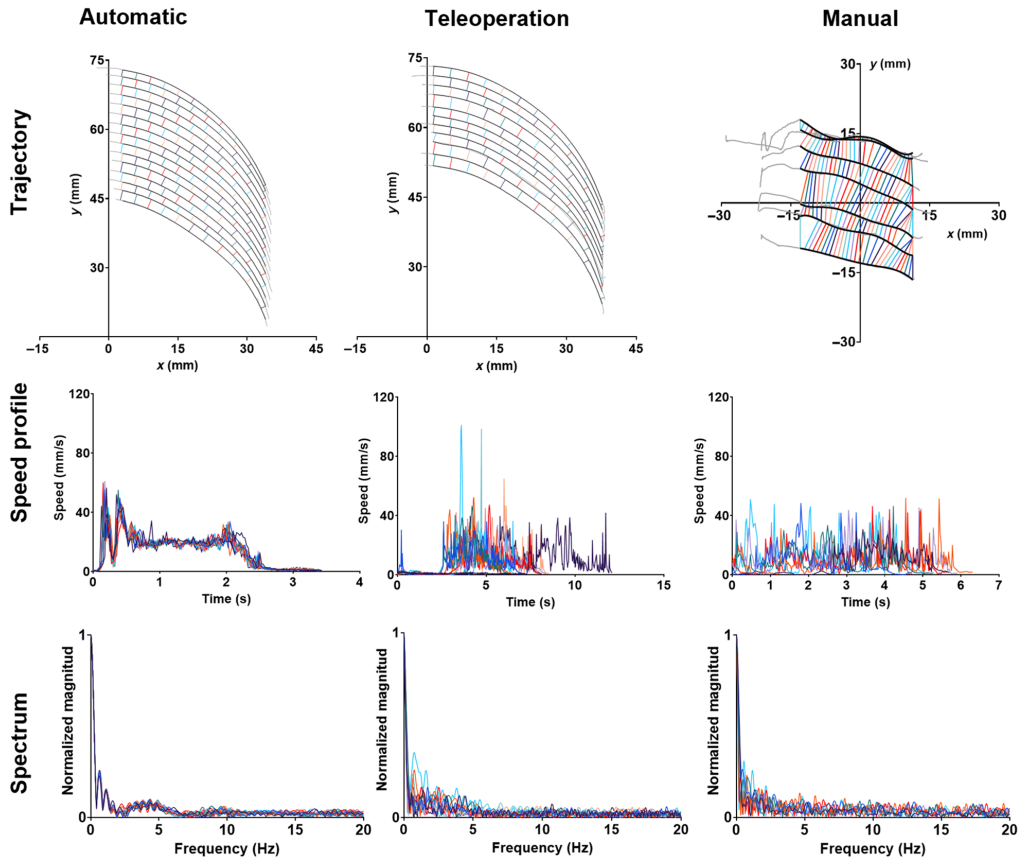
Before performing the scans, the endoscopic system was placed close enough to the target features to ensure the imaging plane was within the imaging range of the OCT system. As a result, the target features were visualized in all 3738, 4883, and 2724 frames obtained during automatic, teleoperation, and manual scanning, respectively, as confirmed *a posteriori* from recorded sequences.

Figure 9 shows the analysis of the EM tracker results obtained in the three experimental setups. Top row shows original positions obtained with the EM tracker during sweep scanning trajectories achieved by bending from 0 deg to 9 deg with 2 mm translation motion parallel to the y-axis. The middle row shows the superposition of the speed profiles corresponding to each sweep and bottom row shows the superposition of the spectral arc lengths for each sweep. In the automatic scanning trajectory 15 curves ( $s_w$ ) were obtained, matching the expected



**Fig. 8** Endoscopic view (left column), top camera view (middle column) and corresponding OCT cross-sectional image (right column) obtained during (a) automatic, (b) teleoperation, and (c) manual scanning of the printed target features. The arrows indicate the dark borders of the ring while the center dark filled circle is indicated with a star.

number of sweeps from the reference trajectory shown in Fig. 5. The total translation was 27.99 mm ( $\Delta T$ ), mean spacing between sweeps 1.54 mm with standard deviation 0.57 mm (noted  $s$ ), and area coverage was 10.11 cm<sup>2</sup>. A spectral arc length ( $\eta_{SAL}$ ) of  $-3.18$  was obtained. The total time of the sweeping trajectory was 46.6s. It can be observed that the speed profile presents an overshoot when transitioning from 0 mm/s to the targeted speed, this is due to non-linearities in the transfer from proximal motor motion to distal tip motion and cable tensioning, which impacts the motor's velocity servoing loop. In the teleoperation mode the operator initially placed the optical device in the first marker line, then performed a sweep trajectory from one side to the another, following the return to the starting position advanced to the next guiding line (2 mm) and repeated the same sweep scanning motion. A total of 11 curves ( $s_w$ ) corresponding to the scanning trajectories were obtained, the total measured translation motion was 21.17 mm ( $\Delta T$ ), the mean of the spacing between trajectories 1.57 mm ( $s$ ) with a standard deviation 0.71 mm, the coverage area was 8.52 cm<sup>2</sup> ( $A$ ) and smoothness ( $\eta_{SAL}$ ) was  $-4.27$ . The total time reached 86.60s. In this mode, the robotized system is continuously receiving new speed and position commands to follow the desired motion driven by the user, so it is expected to observe strong irregularities in the shape of the speed profile in Fig. 9. In the manual scanning data collection, seven curves ( $s_w$ ) corresponding to the scanning trajectories were obtained, the total measured translation motion was 27.5 mm ( $\Delta T$ ), mean of the spacing between trajectories was 4.20 mm ( $s$ ) with a standard deviation of 1.98 mm, the area coverage corresponding to the selected region (see below) was 6.33 cm<sup>2</sup> ( $A$ ) and smoothness ( $\eta_{SAL}$ )  $-5.76$ . The total time was 38.65s. Due to the complex geometry of the plots the fitting curves were computed from the region limited by  $x$ -values  $-11.36$  and 13 mm. This region was selected from the dataset where the scanning curves show less tortuosity and all the computed metrics correspond to this range.



**Fig. 9** Scanning trajectory, speed profile and normalized magnitude of the spectrum of the speed profile for automatic, teleoperation, and manual scanning trajectories.

**Table 2** Summary of metrics.

Metric	Reference	Automatic	Teleoperation	Manual
$\Delta T$ (mm)	28.00	27.99	21.17	27.50
$s$ (mm)	1.31 (0.67)	1.54 (0.57)	1.57 (0.71)	4.20 (1.98)
$s_w$	15	15	11	7
$A$ (cm <sup>2</sup> )	14.68	10.11	8.52	6.33
$\eta_{SAL}$	-2.17	-3.18	-4.27	-5.76
$t$ (s)	3	3.11	7.87	5.52
Motion of endoscope (camera)	—	No	No	Yes

Table 2 summarizes the measured metrics obtained for the three modalities and including the reference trajectory for comparison.

## 4 Discussion

In this paper, we described the capability of a steerable OCT catheter with three DoF to provide extension of the scanning workspace. We proposed a method to quantify scanning performance based on a workspace analysis typically used for robotic devices. The available scanning workspace of most of the OCT imaging devices is limited to translation and rotation of the probe, whereas for our system, the bending capability being a third degree of freedom adds a volumetric

steerability to the workspace. The volumetric scanning workspace was theoretically estimated to be 263 cm<sup>3</sup> and confirmed experimentally to be 255 cm<sup>3</sup>. The proposed experimental validation technique based on an EM tracker is appropriate for a steerable device where the tip position can be measured in space and time. Endoscopic OCT probes are normally used as passive devices that cannot be steered, requiring motion of the entire endoscope to direct the probe. The geometrical model of the steerable OCT device has been presented in this article by adopting knowledge from the robotic field and applying it to the field of endoscopic OCT. The use of this model is relevant for defining feasible scanning trajectories taking advantage of the DoFs of the device without the need of moving the main endoscope during automatic scanning. The steerable capability and the extended scanning workspace of the proposed method can be interesting for improving performance of optical imaging during examination of the colon since the large intestine has a variable diameter that can be up to 9 cm in the cecum and is continuously changing over its length of 1.5 m. Such scanning workspace can also enable microscopic imaging of other organs, such as the stomach. Within the available workspace various scanning trajectories can be selected. To address the problem of margin check during minimally invasive endoscopic treatment we proposed the sweep scanning trajectory, which extended the field of view of the steerable catheter 116 times without the need for motion of the endoscope tip. The 2 mm spacing between each sweep path was chosen to achieve good visibility of the target guiding lines in the endoscopic WL camera image. However, scan separation smaller than 2 mm is possible to perform with the automatic scanning method.

It is important to note that although the distal end optics can be placed at any point in its workspace, the probe beam implements a lateral scan, which is advantageous when imaging flat lesions where the target surface is parallel to the steerable OCT device, making a scanning trajectory based on bending combined with a slower translation motion, as proposed in this article. In the case of pedunculated polyp lesions, the lateral scanning beam could be used to observe the posterior part of the lesion and by combining a translational motion with a slower bending motion in order to follow the shape of the polyp. Open loop scanning is feasible if the target is kept within the depth of field of view during motion. Repositioning the main endoscope can also be used to bring the target inside the visible workspace or to change the angle of the tissue's surface with respect to the B-scan plane.

The preferential way to scan to ensure image quality is to follow the tissue close to its surface without entering into contact with it. Indeed, in case of contact, the behavior of the instrument may become difficult to control because it will depend on unknown parameters such as the stiffness of tissue and frictions parameters. For this purpose, the angle  $\phi$  should indeed be initially tuned to ensure that the plane covered by actuating  $\beta$  and  $\Delta T$  is close to parallel to the tissue's surface. Given the very light weight of the catheter and its stiffness, there is no significant effect of gravity as long as the catheter does not exit the endoscope's channel, which is physically prevented by the relative positioning of the steerable catheter and endoscope at the proximal side.

The rotational speed and the automatic scanning speed must be determined based on appropriate sampling of the target considering the robot capabilities, OCT sampling rate, and its lateral resolution. The circumferential scanning may not be optimal but given the fast acquisition of the OCT system it was not a limiting factor. Future work will focus on finding a good trade-off between smoothness, scanning duration, and rotational speed of the probe.

The automatic scanning trajectory was the most accurate with respect to the reference trajectory and provided the best control of the scanning spacing. Because of subjective visual perception and limited precision of movements, the operator of the teleoperated system and the user of the manual endoscope covered similar scanning areas but with lower number of sweeps (11 and 7 instead of 15), which implies that smaller lesions could be missed in those cases. The automatic scanning was also the fastest, with an average time of 3.11s per sweep, whereas the teleoperation mode was more than two times slower. The manual mode was faster than teleoperation but slower than automatic scanning. The scanning pattern of the manual method was tortuous and nonuniform, still the spectral arc length metric showed good smoothness of the motion. It can be attributed to the excellent skills of the gastroenterologist to navigate the endoscope in a complex geometry of the digestive system. The smoothness of the automatic scanning was the best, which would be crucial for reconstruction of OCT image in post-processing, and its scanning speed can be further increased if necessary.

The endoscopic system used for the telemanipulated and robotic scenarios (Anubiscope from Karl Storz) is different from the conventional endoscope used for the manual scenario. It consists of an endoscope associated with a steerable instrument. The Anubiscope system cannot be operated by a single user, therefore two persons are needed as shown by Diana et al.<sup>59</sup> For this reason and others related to manipulation difficulties, the manual version of the Anubiscope was abandoned by the manufacturer and the robotic version was proposed. On the other hand, the steerable catheter built on the basis of compatibility with the robotic system cannot be currently associated with a standard endoscope because the diameter of conventional working channels is not large enough. The comparison analysis presented in this article was based on the use of the robotic steerable catheter versus conventional manual instrument used in gastroenterology for diagnosis. It must be noted that in the teleoperated and automatic scenarios the main endoscope is not used for controlling the motion of the OCT probe during scanning.

One limitation of this study is the fact that the automatic scanning was performed over a flat target, which provides previous knowledge of the geometry of the sample. This enables capturing high quality data throughout the whole scan thanks to correct positioning of the device at the beginning of the scan. In the case of more complex and unknown tissue geometries, adding closed loop control based on OCT imaging feedback for real time repositioning of the probe with respect to the sample would be needed to realize image acquisition. In the teleoperated and manual modes, correct positioning of the probe was assessed based on the endoscopic and real-time OCT videos.

## 5 Conclusion

The robotization of the steerable endoscopic OCT catheter enabled scanning of a large field of view with improved accuracy. We have presented the geometrical modeling and experimental analysis of the extended scanning workspace enabled by the three DoF, estimated to a volume of 263 cm<sup>3</sup>. This model, originally developed for robotized catheters, was adapted to imaging devices and is compatible with other imaging methods and catheters. A specific automatic scanning trajectory within the available volume, covering an area of 10.11 cm<sup>2</sup>, has been proposed and compared to teleoperation and manual modes. The automatic scanning provided the best trajectory accuracy in comparison with the theoretical reference trajectory. We also proposed the spectral arc length of a speed profile to measure smoothness of motion performed during the whole scanning trajectory. The highest smoothness of motion was achieved for automatic scanning, which shows the potential for uniform OCT image acquisition and the possibility of OCT image frame reconstruction in large area scans. Implementing automatic scanning could allow the doctor to focus on analysis of OCT images for online diagnosis/detection since he/she does not have to control the catheter device. For instance, the operator can have free hands to stop scanning at some point to look more carefully without losing track of the current position.

## Acknowledgments

This work was supported in part by ATIP-Avenir grant; The ARC Foundation; The IdEx Strasbourg University; The European Union's Horizon 2020 research and innovation program under the Marie Skłodowska-Curie grant agreement No 813782 (ATLAS project); ITMO Plan cancer through the INSERM ROBOT project; Investissements d'Avenir program of the French Government, Labex CAMI ANR-11-LABX-0004 and IHU Strasbourg ANR-10-IAHU-02. The authors would like to thank Camille Graf for her assistance during experimental work. The authors declare that there are no conflicts of interest related to this article.

## References

1. J. Fujimoto and E. Swanson, "The development, commercialization, and impact of optical coherence tomography," *Investig. Ophthalmol. Vis. Sci.* **57**, OCT1 (2016).
2. D. Huang et al., "Optical coherence tomography," *Science* **254**, 1178–1181 (1991).

3. A. Pujari et al., "Intraoperative optical coherence tomography guided ocular surgeries: critical analysis of clinical role and future perspectives," *Clin. Ophthalmol.* **14**, 2427–2440 (2020).
4. E. Z. Ahronovich, N. Simaan, and K. M. Joos, "A review of robotic and OCT-aided systems for vitreoretinal surgery," *Adv. Ther.* **38**, 2114–2129 (2021).
5. M. J. Gora et al., "Endoscopic optical coherence tomography: technologies and clinical applications [invited]," *Biomed. Opt. Express* **8**, 2405 (2017).
6. G. J. Tearney et al., "Scanning single-mode fiber optic catheter–endoscope for optical coherence tomography," *Opt. Lett.* **21**, 543 (1996).
7. G. J. Tearney et al., "In vivo endoscopic optical biopsy with optical coherence tomography," *Science* **276**, 2037–2039 (1997).
8. A. M. Rollins et al., "Real-time in vivo imaging of human gastrointestinal ultrastructure by use of endoscopic optical coherence tomography with a novel efficient interferometer design," *Opt. Lett.* **24**, 1358 (1999).
9. X. D. Li et al., "Optical coherence tomography: advanced technology for the endoscopic imaging of barretts esophagus," *Endoscopy* **32**(12), 921–930 (2000).
10. B. Shen et al., "In vivo colonoscopic optical coherence tomography for transmural inflammation in inflammatory bowel disease," *Clin. Gastroenterol. Hepatol.* **2**, 1080–1087 (2004).
11. P. R. Herz et al., "Micromotor endoscope catheter for in vivo, ultrahigh-resolution optical coherence tomography," *Opt. Lett.* **29**, 2261 (2004).
12. W. Kang et al., "Endoscopically guided spectral-domain OCT with double-balloon catheters," *Opt. Express* **18**, 17364 (2010).
13. B. J. Vakoc et al., "Comprehensive esophageal microscopy by using optical frequency-domain imaging (with video)," *Gastrointest. Endosc.* **65**, 898–905 (2007).
14. M. J. Gora et al., "Tethered capsule endomicroscopy enables less invasive imaging of gastrointestinal tract microstructure," *Nat. Med.* **19**, 238–240 (2013).
15. M. S. Smith et al., "Volumetric laser endomicroscopy and its application to barrett's esophagus: results from a 1,000 patient registry," *Dis. Esophagus* **32**, doz029 (2019).
16. J. D. Mosko and D. Pleskow, "Evaluation of NinePoint medical's nvision VLE device for gastrointestinal applications," *Expert Rev. Med. Devices* **14**, 495–503 (2017).
17. K. Liang et al., "Ultrahigh speed en face OCT capsule for endoscopic imaging," *Biomed. Opt. Express* **6**, 1146 (2015).
18. J. A. Izatt and M. A. Choma, "Theory of optical coherence tomography," in *Optical Coherence Tomography*, W. Drexler, J. G. Fujimoto, and A.-H. Dhalla, Eds., Springer, Berlin, Heidelberg, pp. 47–72 (2008).
19. E. Bousi, I. Zouvani, and C. Pitris, "Lateral resolution improvement of oversampled OCT images using capon estimation of weighted subvolume contribution," *Biomed. Opt. Express* **8**, 1319 (2017).
20. M. R. Hee, "Optical coherence tomography of the human retina," *Arch. Ophthalmol.* **113**, 325 (1995).
21. J. S. Schuman, "Quantification of nerve fiber layer thickness in normal and glaucomatous eyes using optical coherence tomography," *Arch. Ophthalmol.* **113**, 586 (1995).
22. L. Huo et al., "Forward-viewing resonant fiber-optic scanning endoscope of appropriate scanning speed for 3D OCT imaging," *Opt. Express* **18**, 14375 (2010).
23. S. Moon et al., "Semi-resonant operation of a fiber-cantilever piezotube scanner for stable optical coherence tomography endoscope imaging," *Opt. Express* **18**, 21183 (2010).
24. A. D. Aguirre et al., "Two-axis MEMS scanning catheter for ultrahigh resolution three-dimensional and en face imaging," *Opt. Express* **15**(5), 2445 (2007).
25. J. M. Zara et al., "Electrostatic micromachine scanning mirror for optical coherence tomography," *Opt. Lett.* **28**, 628 (2003).
26. C.-P.-B. Siu, H. Zeng, and M. Chiao, "Magnetically actuated MEMS microlens scanner for in vivo medical imaging†," *Opt. Express* **15**, 11154 (2007).
27. Q. A. A. Tanguy et al., "A 2-axis MEMS scanning micromirror with a 45° auto-positioning mechanism for endoscopic probe," in *19th Int. Conf. Solid-State Sens., Actuators and Microsyst. (TRANSDUCERS)*, IEEE (2017).

28. S. R. Samuelson et al., "A 2.8-mm imaging probe based on a high-fill-factor MEMS mirror and wire-bonding-free packaging for endoscopic optical coherence tomography," *J. Microelectromech. Syst.* **21**, 1291–1302 (2012).
29. X. Liu et al., "Rapid-scanning forward-imaging miniature endoscope for real-time optical coherence tomography," *Opt. Lett.* **29**, 1763 (2004).
30. K. L. Lurie et al., "Rapid scanning catheterscope for expanded forward-view volumetric imaging with optical coherence tomography," *Opt. Lett.* **40**, 3165 (2015).
31. T.-H. Tsai et al., "Ultrahigh speed endoscopic optical coherence tomography using micro-motor imaging catheter and VCSEL technology," *Biomed. Opt. Express* **4**, 1119 (2013).
32. A. Durrani et al., "Optical rotary junction incorporating a hollow shaft DC motor for high-speed catheter-based optical coherence tomography," *Opt. Lett.* **45**, 487 (2020).
33. T.-H. Tsai, J. Fujimoto, and H. Mashimo, "Endoscopic optical coherence tomography for clinical gastroenterology," *Diagnostics (Basel)* **4**, 57–93 (2014).
34. X. Li et al., "Imaging needle for optical coherence tomography," *Opt. Lett.* **25**, 1520 (2000).
35. L. Zhang et al., "From macro to micro: autonomous multiscale image fusion for robotic surgery," *IEEE Rob. Autom. Mag.* **24**, 63–72 (2017).
36. P. Giataganas et al., "Intraoperative robotic-assisted large-area high-speed microscopic imaging and intervention," *IEEE Trans. Biomed. Eng.* **66**, 208–216 (2019).
37. P. Giataganas, M. Hughes, and G.-Z. Yang, "Force adaptive robotically assisted endomicroscopy for intraoperative tumour identification," *Int. J. Comput. Assist. Radiol. Surg.* **10**, 825–832 (2015).
38. M. Draelos et al., "Automatic optical coherence tomography imaging of stationary and moving eyes with a robotically-aligned scanner," in *Int. Conf. Rob. and Autom. (ICRA)*, IEEE (2019).
39. Y. Li et al., "Automatic montage of SD-OCT data sets," *Opt. Express* **19**, 26239 (2011).
40. J. Yoo et al., "Increasing the field-of-view of dynamic cardiac OCT via post-acquisition mosaicing without affecting frame-rate or spatial resolution," *Biomed. Opt. Express* **2**, 2614 (2011).
41. K. E. Loewke et al., "In vivo micro-image mosaicing," *IEEE Trans. Biomed. Eng.* **58**, 159–171 (2011).
42. K. L. Lurie, R. Angst, and A. K. Ellerbee, "Automated mosaicing of feature-poor optical coherence tomography volumes with an integrated white light imaging system," *IEEE Trans. Biomed. Eng.* **61**, 2141–2153 (2014).
43. M.-H. Laves, L. A. Kahrs, and T. Ortmaier, "Volumetric 3D stitching of optical coherence tomography volumes," *Curr. Directions Biomed. Eng.* **4**, 327–330 (2018).
44. B. Rosa et al., "Building large mosaics of confocal edomicroscopic images using visual servoing," *IEEE Trans. Biomed. Eng.* **60**, 1041–1049 (2013).
45. L. Zorn et al., "A novel telemanipulated robotic assistant for surgical endoscopy: preclinical application to ESD," *IEEE Trans. Biomed. Eng.* **65**, 797–808 (2018).
46. K. M. Horton, F. M. Corl, and E. K. Fishman, "CT evaluation of the colon: inflammatory disease," *Radiographics* **20**, 399–418 (2000).
47. R. J. Webster and B. A. Jones, "Design and kinematic modeling of constant curvature continuum robots: a review," *Int. J. Rob. Res.* **29**, 1661–1683 (2010).
48. S. Balasubramanian, A. Melendez-Calderon, and E. Burdet, "A robust and sensitive metric for quantifying movement smoothness," *IEEE Trans. Biomed. Eng.* **59**, 2126–2136 (2012).
49. S. Estrada et al., "Smoothness of surgical tool tip motion correlates to skill in endovascular tasks," *IEEE Trans. Hum.-Mach. Syst.* **46**, 647–659 (2016).
50. B. Rosa et al., "Intuitive teleoperation of active catheters for endovascular surgery," in *IEEE/RSJ Int. Conf. Intell. Rob. and Syst. (IROS)*, IEEE (2015).
51. A. Devreker et al., "Intuitive control strategies for teleoperation of active catheters in endovascular surgery," *J. Med. Rob. Res.* **1**, 1640012 (2016).
52. K. Waldron and J. Schmiedeler, "Kinematics," in *Springer Handbook of Robotics*, B. Siciliano and O. Khatib, Eds., pp. 9–33, Springer, Berlin Heidelberg (2008).
53. B. Jones and I. Walker, "Kinematics for multisection continuum robots," *IEEE Trans. Rob.* **22**, 43–55 (2006).

54. O. C. Mora et al., “Steerable OCT catheter for real-time assistance during teleoperated endoscopic treatment of colorectal cancer,” *Biomed. Opt. Express* **11**, 1231 (2020).
55. F. Nageotte et al., “Stras: a modular and flexible telemanipulated robotic device for intraluminal surgery,” in *Handbook of Robotic and Image-Guided Surgery*, M. H. Abedin-Nasab, Ed., pp. 123–146, Elsevier (2020).
56. I. C. B. H. Anton and S. Davis, *Calculus*, 10th ed., Houghton Mifflin Harcourt Publishing Company (2012).
57. P. Cignoni et al., “MeshLab: an open-source mesh processing tool,” in *Eurographics Italian Chapter Conf.*, V. Scarano and R. D. Chiara and U. Erra, Eds., The Eurographics Association (2008).
58. C. B. Barber, D. P. Dobkin, and H. Huhdanpaa, “The quickhull algorithm for convex hulls,” *ACM Trans. Math. Software* **22**, 469–483 (1996).
59. M. Diana et al., “Endoluminal surgical triangulation: overcoming challenges of colonic endoscopic submucosal dissections using a novel flexible endoscopic surgical platform: feasibility study in a porcine model,” *Surg. Endosc.* **27**, 4130–4135 (2013).

Biographies of the authors are not available.